

## Article

# An Analysis of Mobility Influence in Optoelectronics Parameters in an InGaN/GaN Blue LED

Sarai Zarate-Galvez <sup>1</sup>, Abel Garcia-Barrientos <sup>2,\*</sup>, Roberto Ambrosio-Lazaro <sup>3</sup>, Mario Garcia-Ramirez <sup>4</sup>, Enrique Stevens-Navarro <sup>2</sup>, Jairo Plaza-Castillo <sup>5</sup>, Jose Hoyo-Montaña <sup>6</sup> and Obed Perez-Cortes <sup>7</sup>

<sup>1</sup> Instituto de Investigación en Comunicación Óptica, Universidad Autónoma de San Luis Potosí, San Luis Potosí 78210, Mexico

<sup>2</sup> Faculty of Science, Universidad Autónoma de San Luis Potosí (UASLP), San Luis Potosí 78295, Mexico

<sup>3</sup> Faculty of Electronics, Benemerita Universidad Autónoma de Puebla, Puebla 72000, Mexico

<sup>4</sup> Research Centre for Applied Science and Engineering, UDG, Guadalajara 44100, Mexico

<sup>5</sup> Department of Physics, Universidad del Atlántico, Barranquilla 081008, Colombia

<sup>6</sup> Department of Electronics, Instituto Tecnológico de Hermosillo, Hermosillo 83170, Mexico

<sup>7</sup> Área Académica de Computación y Electrónica, Universidad Autónoma del Estado de Hidalgo, Mineral de la Reforma 42184, Mexico

\* Correspondence: abel.garcia@uaslp.mx



**Citation:** Zarate-Galvez, S.;

Garcia-Barrientos, A.;

Ambrosio-Lazaro, R.; Garcia-Ramirez,

M.; Stevens-Navarro, E.;

Plaza-Castillo, J.; Hoyo-Montaña, J.;

Perez-Cortes, O. An Analysis of

Mobility Influence in Optoelectronics

Parameters in an InGaN/GaN Blue

LED. *Crystals* **2022**, *12*, 1108. [https://](https://doi.org/10.3390/cryst12081108)

[doi.org/10.3390/cryst12081108](https://doi.org/10.3390/cryst12081108)

Academic Editors: Hao-chung Kuo and Ikai Lo

Received: 2 July 2022

Accepted: 4 August 2022

Published: 8 August 2022

**Publisher's Note:** MDPI stays neutral with regard to jurisdictional claims in published maps and institutional affiliations.



**Copyright:** © 2022 by the authors. Licensee MDPI, Basel, Switzerland. This article is an open access article distributed under the terms and conditions of the Creative Commons Attribution (CC BY) license (<https://creativecommons.org/licenses/by/4.0/>).

**Abstract:** Simulations on mobility influence in optoelectronics parameters from an InGaN/GaN blue LED using the Nextnano++ software are presented in this paper. These simulations were performed by changing the hole and electron mobility value for the material compounds according to experimental, theoretical, and doping-concentration data already reported in the literature. The power law mobility is used for the current calculation in the quantum drift-diffusion model. The results indicate the lower hole and electron leakage currents correspond to the lowest mobility values for the InGaN alloy, the greatest amount of recombination occurs in the extreme wells within the active layer of the LED and the stable emission is at 3.6 V with peak wavelength  $\lambda_{LED} = 456.7$  nm and full width at half maximum  $FWHM \sim 11.1$  nm for the three mobilities. Although experimental and theoretical mobility values reach higher carrier density and recombination, the photon emission is broader and unstable. Additionally, the doping-concentration mobility results in lower wavelength shifts and narrows FWHM, making it more stable. The highest quantum efficiency achieved by doping-concentration mobility is only in the breakdown voltage ( $\eta_{dop-max} = 60.43\%$ ), which is the IQE value comparable to similar LEDs and is more useful for these kinds of semiconductor devices.

**Keywords:** InGaN/GaN; blue light emitting diodes; quantum efficiency; quantum drift-diffusion model

## 1. Introduction

The simulation of semiconductor devices using the Quantum Drift Diffusion (QDD) model is one of the most widely used and useful mathematical methods for describing electronic transport at the nano-scale [1–3]. Due to the enormous importance of Light-Emitting Diodes (LEDs) today, it is necessary to employ computational techniques to predict their optoelectronics performance prior to small- or large-scale manufacture. InGaN/GaN Multiple-Quantum-Well (MQW) light-emitting diodes have many uses in, communications, electronics, chemistry, and the lighting industry over the world [4–8]. Therefore, it is of maximum importance. Numerical simulations of LEDs using the QDD model have been performed to understand and predict the behavior of different physical variables, as well as to optimize the multiple-quantum wells number, to design the band structures in the device and explore new arrangements of heterostructures [9–11]. The important parameters set out by previous studies are the Shockley-Read-Hall (SRH) recombination lifetime, Auger recombination coefficient, and percentage of the polarization charge density, among others. There are three studies [9–11] sharing the following simulation characteristics: temperature

at 300 K, 1D simulation, but no mention is made of the mobility model used or the value of the latter parameter. The mobility model ( $\mu$ ) is important because it can change the output physical variables and the device performance, although some authors do not attach importance to it [12]. To demonstrate the relevance of the mobility model and its values for the holes and electron transport ( $\mu_h$ ,  $\mu_e$ ), in this paper we study the mobility influence in optical and electrical parameters from a InGaN/GaN blue LED using the QDD model on the Nextnano++ software. This software has been successfully used to investigate different nanostructures [13–16]. In this work, three simulations varying the mobility values were carried out: one using experimental values, another taking theoretical values, and the last one taking mobility values depending on doping-concentration of the semiconductor device. The simulation results using experimental value mobility were taken as a reference to compare the theoretical and doping-concentration mobility modeling. This study also compares the spatial current distribution, carrier density, recombination processes, emission spectrum, and quantum efficiency to generate a comprehensive view of the device parameters.

## 2. Device Structure and Material Parameters

The most common LED structure has between one and five quantum wells (QWs) [9,10], but in this study, four QWs were chosen and a flat simple structure in c-plane direction of a wurtzite crystal was selected. The active layer is a compound of 3 nm thick  $In_{0.15}Ga_{0.85}N$  QWs interleaved by a 12 nm thick GaN barrier layer. The active layer is confined by 3.5  $\mu\text{m}$  *n*-type and 150 nm *p*-type GaN, and at the ends, ohmic contacts complete the device, as is shown in Figure 1. Electron and hole concentrations of the doped semiconductors are  $n\text{-GaN} = 1 \times 10^{17} \text{ cm}^{-3}$  and  $p\text{-GaN} = 1 \times 10^{19} \text{ cm}^{-3}$ , respectively. The purpose of having a high *p* is to decrease the ionization energy of acceptors [17,18] and increase the hole injection towards the farthest quantum wells of the *p*-GaN layer [9]. This is because under typical growth conditions, hexagonal GaN has an intrinsic *n*-type nature [19,20]. An Electron Blocking Layer (EBL) was not added to the structure to keep it simple and avoid the potential barrier for holes that it generates [11]. Instead, a low electron concentration was chosen to reduce electron leakage [21].

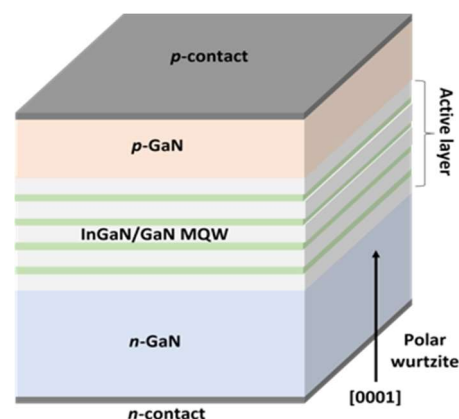


**Figure 1.** Schematic illustration of InGaN/GaN blue LED structure.

In this research work, the optical and electrical properties of blue LED structure, shown in Figure 1, are numerically investigated using the Nextnano++ software. This self-consistently solves the Poisson equation, Schrödinger equation and the drift-diffusion model for the carrier transport with suitable boundary conditions. Equations are discretized using a box integration finite difference approach to take material discontinuities into account. Given the optoelectronic nature of the device, the electron-hole pair generation-recombination processes within the active layer of the diode considered were: (1) Shockley-Read-Hall, (2) Auger, and (3) radiative [11,22]. In addition, the hexagonal and asymmetric crystalline base in the device generates a dipole in the unit cell [23–25]. There-

fore, spontaneous (SP) and piezoelectric polarizations (PZ) appear in the material [26–28]. Additionally, the indium incorporation into the InGaN alloy increases the unit cell size triggering strain between the GaN/InGaN interfaces [29]. All these mismatches in the lattice produce band structure shifts in the device. However, they can be included in the equations as deformation potentials, so during the simulation a “strain” equation solution was included.

To solve the continuity and carrier transport equations, a constant low-field mobility model (also called the power law mobility model) [30–32] is used for the current calculation. For the simulations, the difference between electron and hole transport is represented by electron/hole mobility ( $\mu_h$ ,  $\mu_e$ ) for both binary precursor compounds, InN and GaN. Table 1 lists the values of experimental, theoretical, and doping-concentration mobilities taken from literature. Because the dopant concentration only changes in GaN material, the electron and hole mobility for InN was fixed using the theoretical mobility. In this case, six mobility profiles corresponding to electron (three) and hole (three) calculations will be produced. These profiles represent the abrupt changes of material along the device. These profiles are labeled to depict the three simulations analyzed in this study as:  $\mu_{e/h-exp}(x)$ ,  $\mu_{e/h-theo}(x)$ ,  $\mu_{e/h-dop}(x)$  for the experimental, theoretical and doping-concentration mobilities, respectively. The numerical results generated by the experimental mobility values were taken as a reference for the analysis of the other simulations.

**Table 1.** Mobility values for binary precursor compounds of the InGaN/GaN blue LED.

Binary Compound	Mobility [ $\text{cm}^2/\text{V}\cdot\text{s}$ ]		
	Experimental	Theoretical	Doping Concentration
GaN	$\mu_e = 1265$ [33]	$\mu_e = 905$ [34]	$\mu_e = 1035$ [35]
	$\mu_h = 31$ [36]	$\mu_h = 44$ [34]	$\mu_h = 30$ [19]
InN	$\mu_e = 2000$ [37,38]	$\mu_e = 3200$ [39]	<sup>1</sup> $\mu_e = 3200$ [39]
	$\mu_h = 39$ [40]	$\mu_h = 220$ [41]	<sup>1</sup> $\mu_h = 220$ [41]

<sup>1</sup> Electron and hole mobility for InN was fixed using theoretical mobility.

The conduction bands are assumed to be decoupled from valence sub-bands due to the wide bandgap of GaN, so the single-band effective mass approximation is employed for the Gamma conduction band. To avoid numerical constraints during simulations, the single-band Schrödinger equation was solved for the heavy-hole (HH), light-hole (LH), and spin-orbit (SO) valence bands. Other basic parameters for simulations are the following: a variable spatial grid on 1D in the entire device was employed, as shown in Figure 2; for the 150 nm n-GaN and p-GaN the spatial resolution was  $\Delta x = 10$  nm, and for the active layer,  $\Delta x = 0.1$  nm; a voltage sweep was made from 0 to 4.1 Volts with a step of  $\Delta V = 0.05$  V (The choice of the voltage end point corresponds to the point where the simulation convergence starts to become hard, which corresponds to the forward voltage point); the SRH lifetime ( $\tau_{SRH}$ ), the Auger recombination coefficient ( $C_{Auger}$ ) and radiative recombination coefficient ( $B_{rad}$ ) for electrons and holes, were fixed at 1 ns [42],  $1 \times 10^{-30}$   $\text{cm}^6/\text{s}$  [43] and  $2 \times 10^{-10}$   $\text{cm}^3/\text{s}$  [44,45], respectively, for both binary precursors; and the simulation temperature was 300 K.

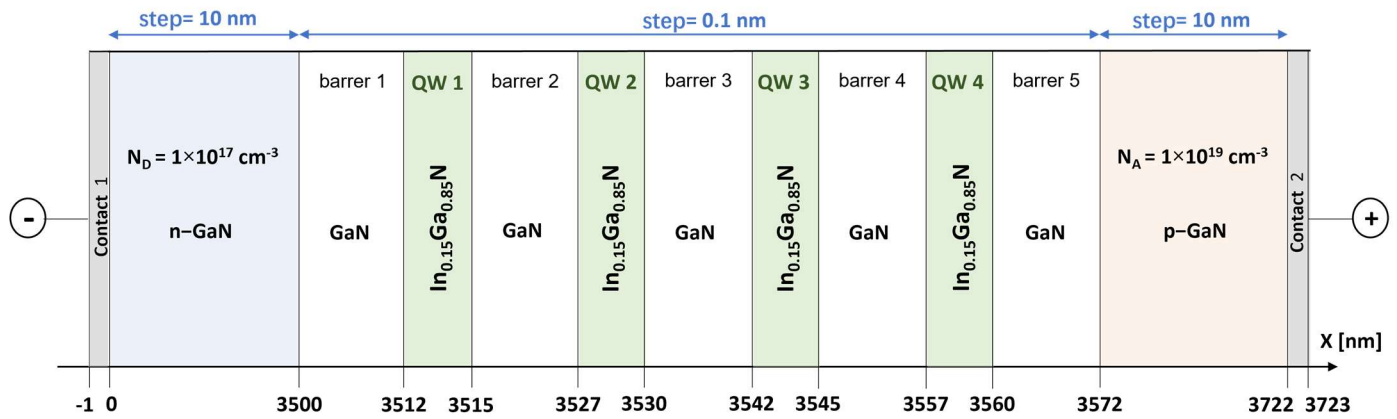


Figure 2. Simulation spatial diagram and parameters for the InGaN/GaN blue LED.

### 3. Results

Figure 3 shows the hole and electron mobility profile ( $\mu_{e/h-exp}$ ,  $\mu_{e/h-theo}$ ,  $\mu_{e/h-dop}$ ) according to the different materials within the active layer of the LED. Compared with the GaN material, both plots indicate a higher mobility for the InGaN. For holes, the theoretical mobility ( $\mu_{h-theo}$ ) reaches the highest value and the experimental mobility ( $\mu_{h-exp}$ ) the lowest within the wells. For electrons, the experimental mobility ( $\mu_{e-exp}$ ) is higher and the theoretical mobility ( $\mu_{e-theo}$ ) lower.

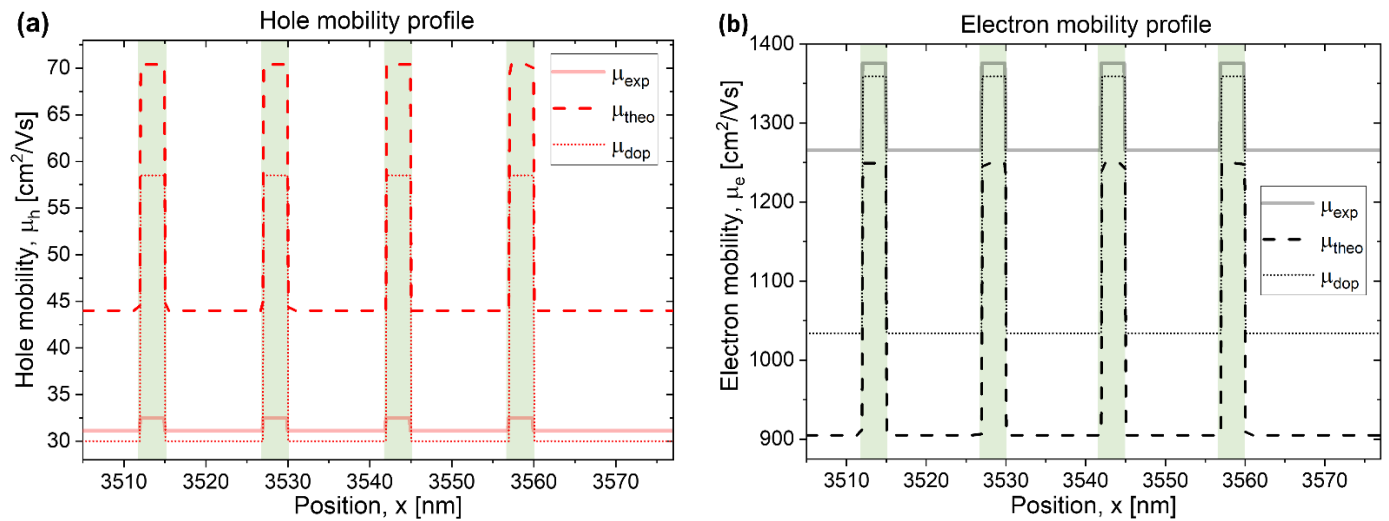
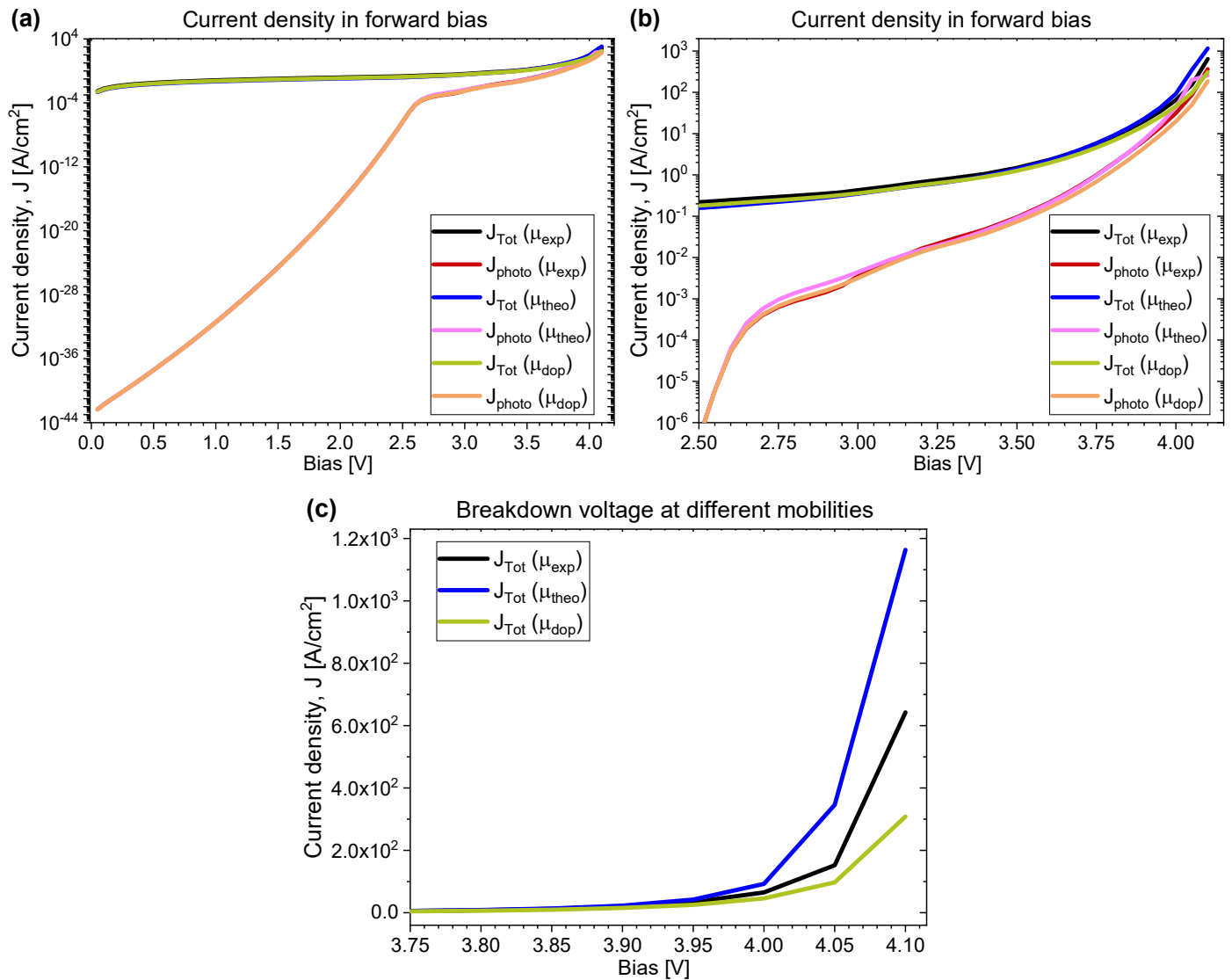


Figure 3. (a) Hole and (b) electron mobility profile according to Equation (1) using a constant low-field mobility model for the simulated LED.

Figure 4a shows the J-V curves for the three mobility cases in forward bias between (0–4.1) V. Figure 4b is an extension of the interest zone corresponding to (2.5–4.1) Volts where the slope changes in lines indicate changes in the transport and the emergence of recombination mechanisms within the device. The latter voltage range is where a more meaningful comparison can be made of changes for different physical parameters in the LED, such as spatial current distribution, carrier density, recombination processes, emission spectrum and quantum efficiency. In Figure 4b, the total current density ( $J_{tot}$ ) and photocurrent ( $J_{phot}$ ) for the doping-concentration mobility simulation remains below the theoretical and experimental mobility curves as the voltage increases. Compared to experimental and doping-concentration results,  $J_{tot}$  for the theoretical simulation reaches the highest values in the last volt from computation. In contrast, the experimental and theoretical photocurrents are almost identical for most of the voltage points. Figure 4c shows the breakdown voltage ( $V_b$ ) for the three different mobilities ( $V_{b-exp} = 4.00$  V,  $V_{b-theo} = 4.05$  V,

$V_{b-dop} = 4.10$  V). A similar structure of InGaN/GaN blue LED was reported exhibiting a breakdown voltage of 3.65 V [46]; thus, these results are comparable. Although the breakdown voltage of today's commercial blue LEDs is generally about 3 V, or even lower than 3 V [9,11,21], this is because the electron concentration of n-GaN is usually more than  $10^{18} \text{ cm}^{-3}$  [11,12,42,47,48], i.e., more than 10 times the electron concentration of this study. Having a low electron concentration, the n-GaN semiconductor is more intrinsic, and the Fermi level is further away from the conduction band edge, so a higher voltage is required to turn it up and cause electrons to begin to pass into the conduction band. Consequently, the breakdown voltage is shifted towards higher voltages.



**Figure 4.** ( $J$ – $V$ ) curves in forward bias: (a) from [0–4] V in logarithmic scale, (b) the magnification between [2.5–4.1] V in logarithmic scale, and (c) breakdown voltage of the simulated LED.

Analysis of the physical parameters of the LED was performed for four different voltages points (2.5 V, 3.0 V, 3.5 V, 4.0 V) where the photocurrent rises. Figure 5 corresponds to the spatial distribution current and density carrier results inside the active layer from the device at 2.5 V. In Figure 5a, hole and electron density currents are not reduced in quantum wells. Here, it can be seen that the hole current density for experimental, theoretical, and doping-concentration simulations have a magnitude of almost zero ( $J_h = -(3.5 - 5.3) \times 10^{-4} \text{ A/cm}^2$ ). However, the electron current density presents significant differences. In ascending order the values are:  $J_{e-theo} = -(1574.84 \pm 0.07) \times 10^{-4} \text{ A/cm}^2$ ,

$J_{e-dop} = -(1797.01 \pm 0.12) \times 10^{-4} \text{ A/cm}^2$  and  $J_{e-exp} = -(2186.56 \pm 0.14) \times 10^{-4} \text{ A/cm}^2$ . At this voltage point the electric field is too low to drag the electrons into the wells ( $n$  is the constant black line at  $n = 0$  in Figure 5b). In contrast, if the hole density has tunneled the active layer and accumulates in the closest well to n-side, this is a consequence of the large difference between the number of electrons and holes concentration and the diffusion process in the device. The *Relative Percentage Difference (RPD)* parameter is the relative error used to quantify the changes in physical variables for each simulated mobility with respect to the experimental, as shown in Equation (1).

$$RPD_{exp-theo,dop} = \frac{|(Y)_{exp} - (Y)_{theo,dop}|}{(Y)_{exp}} \times 100 \quad (1)$$

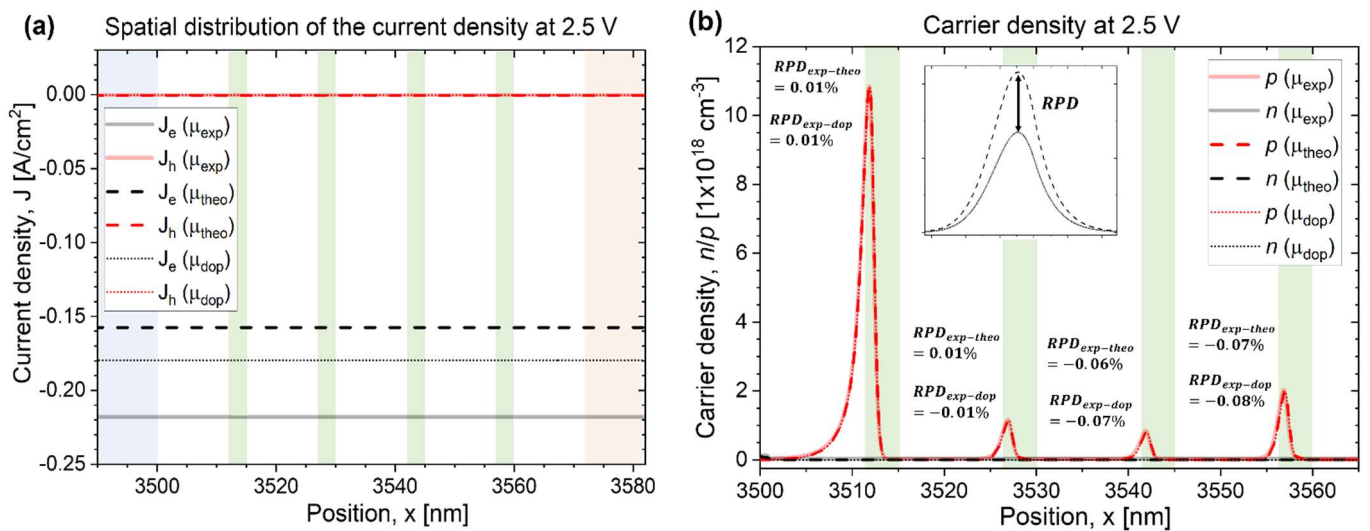


**Figure 5.** (a) Spatial distribution of current density and (b) carrier density in the active layer of the LED at 2.5 Volts.

In Figure 5b, the hole density plot with experimental mobility is higher than the theoretical and doping-concentration mobility curves in the last two wells and slightly lower only for the first well. The *RPD* declined to 0.1% in the four wells; therefore, at this voltage there are no significant changes in the carrier density between the three mobilities. The negative sign in percentages indicate a reduction of carrier density with respect to the experimental mobility simulation.

Figure 6 corresponds to  $V = 3$  volts. As shown in (a), the hole and electron currents are being consumed in each well because of the recombination between electrons and holes crossing the GaN quantum barriers. In this graph “the leakage current”  $j_{leak}$  can be observed, and some electrons pass through the active layer without recombining, due to their low effective mass; on the other hand, the holes are almost entirely recombined. Here, the theoretical simulation reveals a lower electron leakage ( $j_{leak-theo} = 64.93\%$ ,  $j_{leak-dop} = 72.20\%$  and  $j_{leak-exp} = 74.33\%$ ) and the experimental simulation a lower hole leakage ( $j_{leak-theo} = 1.12.93\%$ ,  $j_{leak-dop} = 0.94\%$  and  $j_{leak-exp} = 0.83\%$ ). The theoretical and doping-concentration hole densities rise with respect to the experimental, especially in QW2 ( $RPD_{exp-theo} = 11.86\%$ ,  $RPD_{exp-dop} = 2.24\%$ ) and QW3 ( $RPD_{exp-theo} = 9.64\%$ ,  $RPD_{exp-dop} = 3.30\%$ ), as shown Figure 5b. The above is in accordance with the values shown in Figure 3a, where theoretical and doping-concentration mobility values for holes in the InGaN wells are higher than the experimental values. The electron density (Figure 6c) indicates more electron accumulation in the first three QWs for the theoretical mobility, the experimental mobility shifts the electrons to the last three QWs, and the doping-concentration mobility is agglomerated in the two intermediate QWs. This can be explained by referring to Figure 3b where the theoretical mobility for electrons is lower than the other mobilities; therefore, most of

them lag in the first wells. Instead, as the experimental mobility is the highest, a very large number of electrons are injected into the wells closer to the  $p$ -side of the device, as mentioned by Dong [21]. The three simulations agree that most of the electrons accumulate in well QW3. The  $RPD$  parameter states that the theoretical electron concentration rises with respect to the experimental, having its highest value in QW1 ( $RPD_{exp-theo} = 60.37\%$ ). The electron density by doping-concentration remains below the experimental simulation in the four wells, reaching its largest difference in QW4 ( $RPD_{exp-dop} = -23.33\%$ ), where it acquires the same density value as the theoretical simulation.

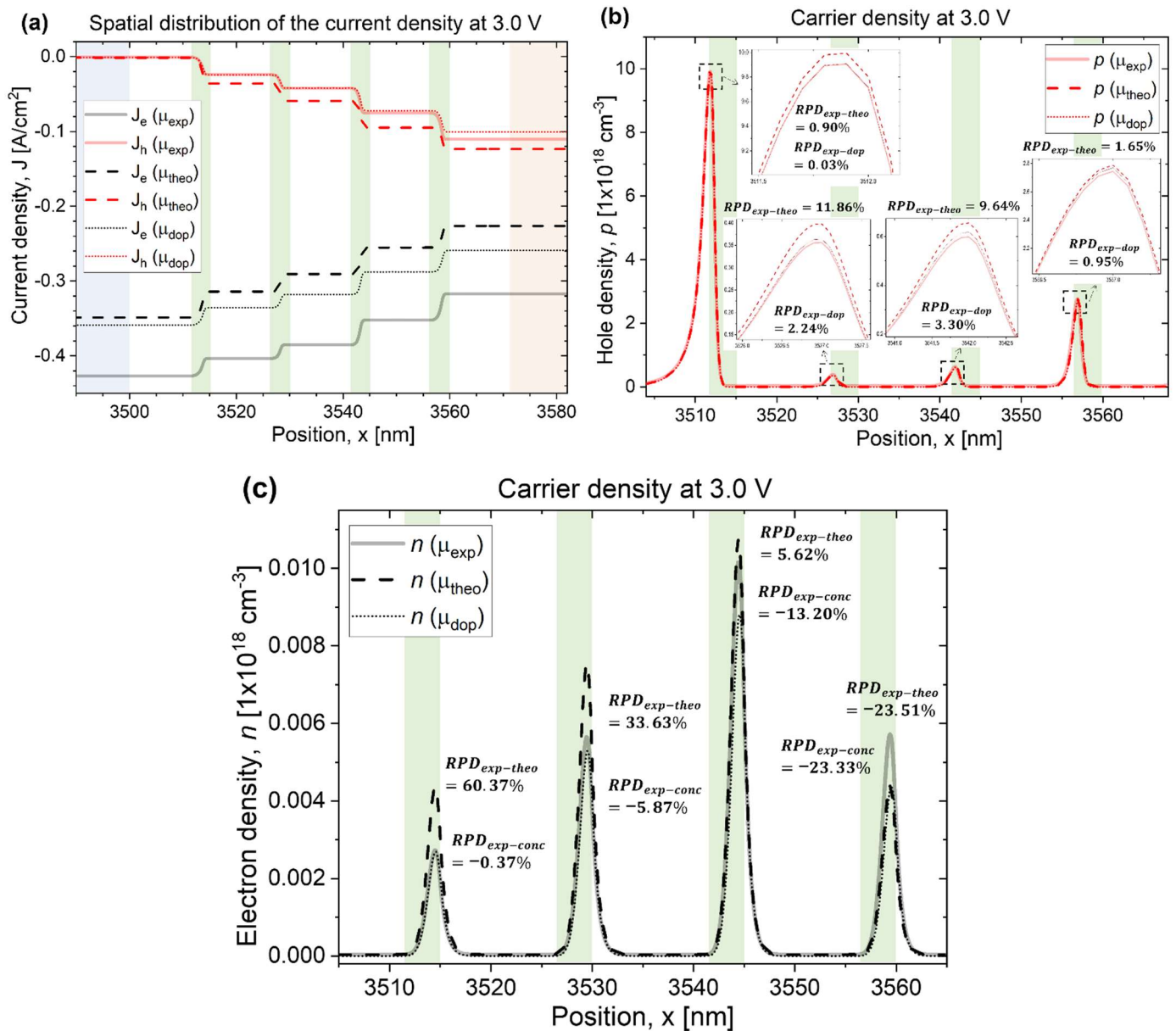


**Figure 6.** (a) Spatial distribution of current density, (b) hole, and (c) electron density in the active layer of the LED at 3.0 Volts.

Figure 7 refers to 3.5 V, displaying in (a) the spatial distribution of current, as well as the hole ( $j_{leak-theo} = 4.29\%$ ,  $j_{leak-dop} = 3.40\%$  and  $j_{leak-exp} = 2.77\%$ ) and electron ( $j_{leak-exp} = 23.76\%$ ,  $j_{leak-dop} = 22.91\%$  y  $j_{leak-theo} = 18.15\%$ ) leakage. The lowest leakage currents correspond to the lowest values of hole and electron mobility inside the quantum wells (See Figure 3). This indicates that a lower mobility for the InGaN alloy favors the energy dispersion in the form of photons by electron/hole (e/h) recombination. That is, if

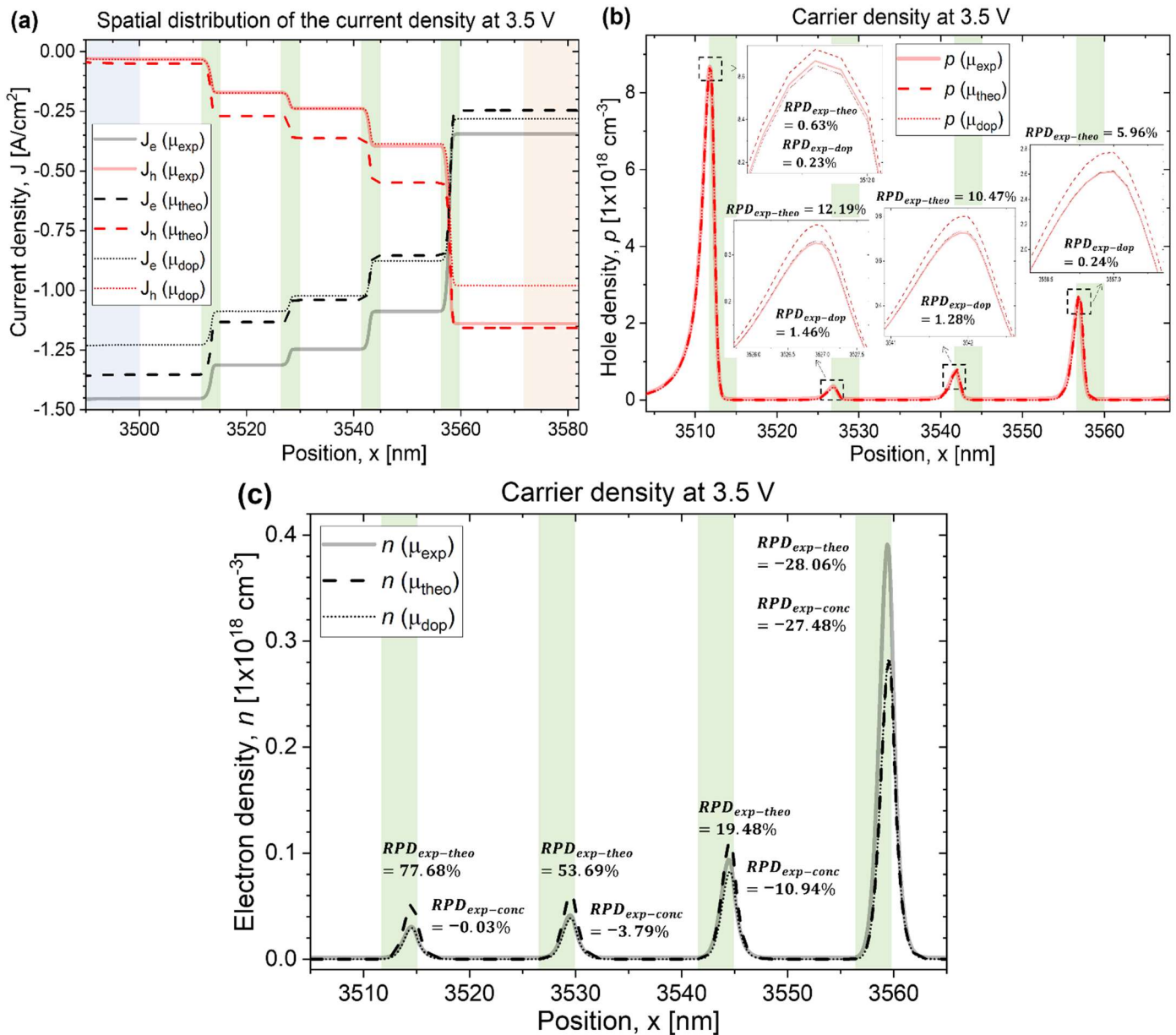
$\mu_1 < \mu_2$  and using the semiclassical equation  $\mu_i = q\langle\tau_i\rangle\hat{m}^{-1}$ , then  $\langle\tau_1\rangle < \langle\tau_2\rangle \therefore \frac{1}{\langle\tau_1\rangle} > \frac{1}{\langle\tau_2\rangle}$ , where  $\frac{1}{\langle\tau_i\rangle}$  is the “scattering rate”. In Figure 7b, again the hole density for the theoretical and doping-concentration mobility increases with respect to the experimental, although the concentration mobility simulation remains very close to the experimental curve. The hole density for the theoretical simulation has a slight gain in the  $RPD$  values for QW2 ( $RPD_{exp-theo} = 12.19\%$ ) and QW3 ( $RPD_{exp-theo} = 10.47\%$ ) compared with the previous voltage, but the higher gain is in QW4 ( $RPD_{exp-theo} = 5.96\%$ ). The electron density (Figure 7c) shows an increment in the  $RPD_{exp-theo}$  for all wells, with QW1 having the highest value ( $RPD_{exp-theo} = 77.68\%$ ). In addition, it is evident that the distribution profile has shifted to the  $p$ -side of the device with respect to the above voltage. This is a consequence of the increase in the electric field driving most of the electrons into the QW4 for the three simulations. The electron density for the experimental mobility remains predominant in the latter well, which may be attributed to the high value of the experimental electron mobility per se. The  $RPD_{exp-dop}$  values decrease very little for the first two wells but the differences increase in QW4 ( $RPD_{exp-dop} = -27.48\%$ ). At this voltage point, the differences in mobility values between simulations and theoretical and experimental values, and doping-concentration are appreciable.

Figure 8 presents the last voltage point (4.0 V), at which the hole leakage currents were  $j_{leak-theo} = 12.38\%$ ,  $j_{leak-dop} = 8.42\%$ , and  $y_{j_{leak-exp}} = 7.29\%$ . The electron leakage currents were  $j_{leak-dop} = 0.75\%$ ,  $j_{leak-exp} = 0.65\%$ , and  $y_{j_{leak-theo}} = 0.35\%$ . This data reiterates that lower mobility for the InGaN alloy favors the permanence of e/h pairs and their recombination within the well. Figure 8b clearly shows a large difference in hole density between simulations, which is evident in the high  $RPD$  values in each well. Here, the highest hole density is reversed, from QW1 to QW4. An increase in the density magnitude is seen for all wells, contrary to what was occurring previously where the hole density within the LED active layer was decreased by the recombination processes as the voltage increased. This indicates that the threshold injection has been reached, which means that continuing to supply the electric field will break the device, as indicated by Figure 4c. The simulation with doping-concentration mobility decreases greatly with respect to the experimental curve, reaching its greatest difference in QW4 ( $RPD_{exp-dop} = -17.50\%$ ). Hole density simulation with theoretical mobility increases greatly and has the highest  $RPD$  in QW2. In Figure 8c, electron density continues to increase in QW4, and also within the other wells, it reaches higher magnitudes than previously, even higher than the electron concentration in  $n$ -GaN. That the magnitude of electrons increases this much can be understood by considering that the intense potential detaches electrons from deeper layers (bound states) of the material. The  $RPD$  values for this graph are the highest obtained, which demonstrates that there is a substantial difference between simulations when a simple and constant value such as the mobility is changed.

As is seen from Figures 5–8, the large difference between hole and electron concentrations used in this study ( $p$ -GaN/ $n$ -GaN = 100) helps to obtain low leakage currents at high voltage points, which is advantageous compared with several commercial LEDs, and represents an electronic overflow or insufficient hole injection. It was demonstrated that with an appropriate choice of  $n$ -type and  $p$ -type dopants, the optoelectronic properties of LEDs can be improved, especially the distribution of electrons and holes in the MQWs.

Figure 9 shows the dynamics of carrier recombination. First, around 2.5 V, the increase in recombination processes consumes holes in the first well, where most of them accumulate. As the electric field increases, recombination continues mainly in QW1 and it is extended into the other three wells, but noticeably more in the last one (~3.0 V). Then, the presence of electrons in QW4 attracts a larger number of holes to the same well, increasing recombination in it, since only one quantum barrier must be overcome there at 3.5 V. Finally, at 4.0 Volts, almost all recombination takes place in QW4. Although the three recombination processes (SRH, Auger, radiative) consume e/h pairs, radiative recombination is the main source of photons. For this reason, only the radiative recombination rate is presented in Figure 9. For reasons of clarity, the graph is not to scale. In agreement with the previous

analysis, Table 2 shows the  $RPD$  for  $R_{rad}$  between simulations in all analyzed voltage points. An important aspect of Figure 9 is that the recombination in the intermediate wells is maintained below 17% of total recombination in the four wells, compared with QW1 and QW4, which together amount to more than 83% of the total recombination at any voltage point. This shows that the recombination is distributed in the extreme wells of the active layer; hence, many QWs do not represent an advantage when a LED is designed as indicated by S. Lu [47]. This may also be caused by an incorrect choice of the Auger recombination coefficient, which changes the spatial distribution of radiative recombination in the LED as is shown by J. R. Cheng [48].



**Figure 7.** (a) Spatial distribution of current density; (b) hole and (c) electron density in the active layer of the LED at 3.5 Volts.

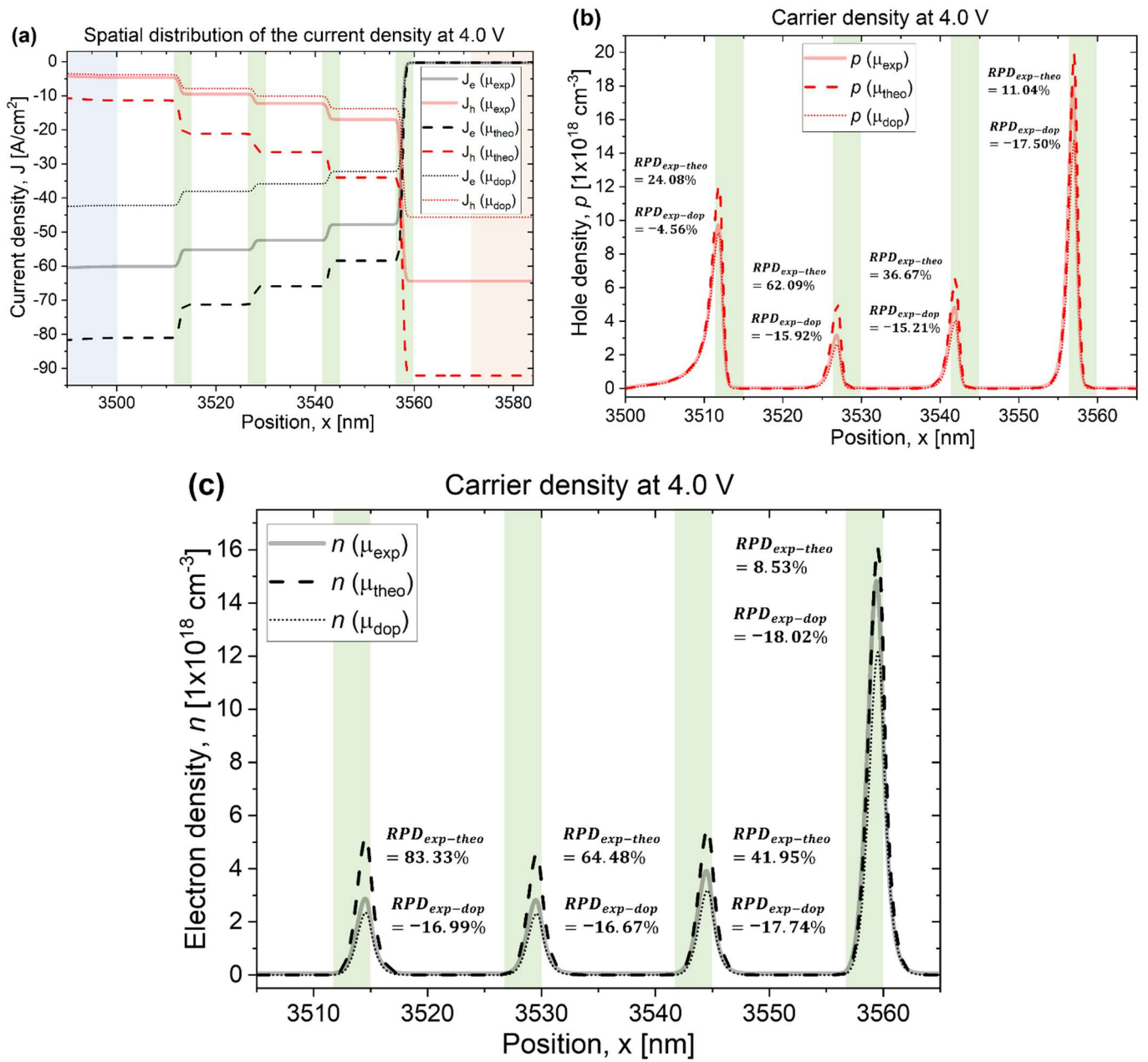
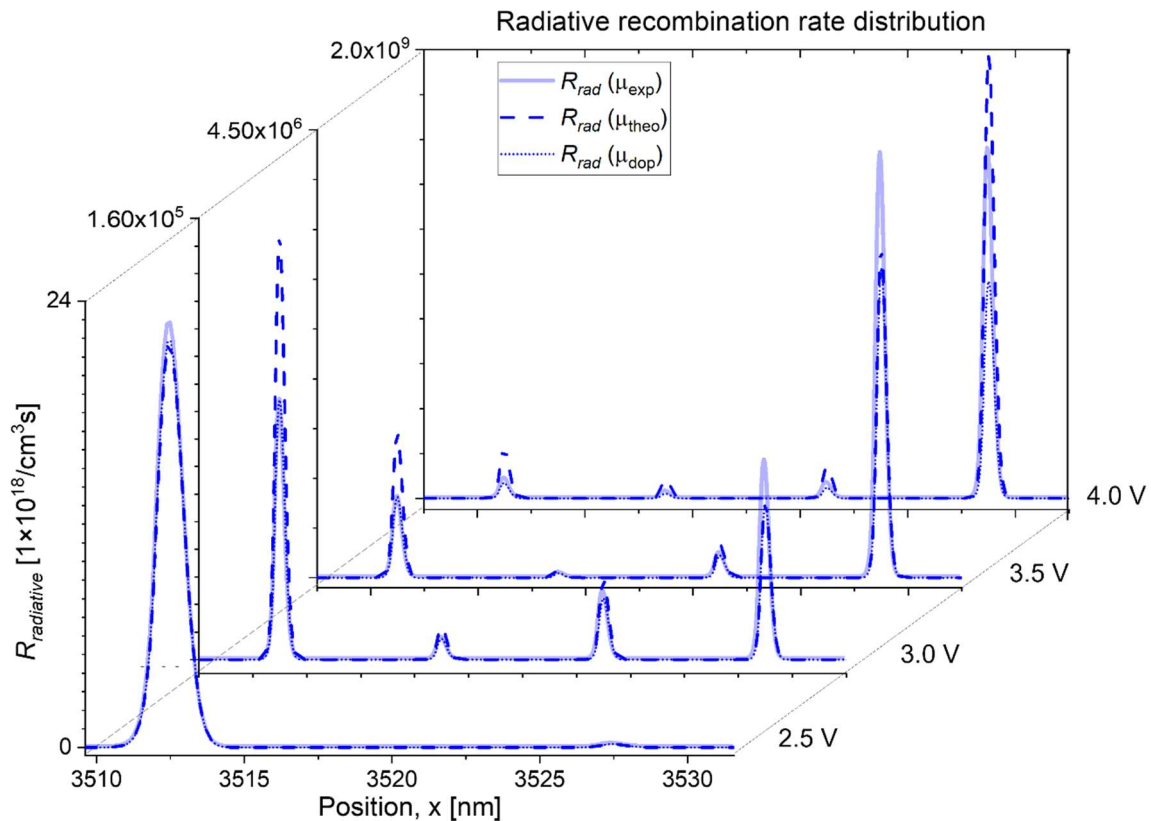


Figure 8. (a) Spatial distribution of current density, (b) hole, and (c) electron density in the active layer of the LED at 4.0 Volts.

Table 2. Relative Percentage Difference for radiative recombination from In<sub>0.15</sub>Ga<sub>0.85</sub>N/GaN at different voltage points.

<i>R<sub>rad</sub></i>	2.5 V		3.0 V		3.5 V		4.0 V	
	<i>RPD<sub>exp-theo</sub></i> [%]	<i>RPD<sub>exp-dop</sub></i> [%]						
QW1	-5.04	-4.12	62.51	-0.15	79.00	-0.43	152.93	-22.50
QW2	-4.79	-4.01	50.23	-3.85	72.83	-2.51	185.05	-31.14
QW3	—	—	16.77	-10.21	32.62	-9.86	104.17	-31.93
QW4	—	—	-21.35	-22.40	-22.82	-27.19	26.27	-38.01



**Figure 9.** Spatial distribution of the radiative recombination rate for 2.5 V, 3.0 V, 3.5 V and 4.0 V voltage points of the LED.

The number of photons emitted in the recombination is counted and distributed according to the wavelength recorded (Figure 10). For analysis of these spectra, the spontaneous emission of each photon is assumed as a Lorentzian shape. Figure 10a corresponds to 2.5 V and shows the emission spectrum is centered in the same wavelength for the three simulations ( $\hat{\lambda}_{exp} = \hat{\lambda}_{theo} = \hat{\lambda}_{dop} = 458.4$  nm) with an almost identical FWHM. At 3.0 V, the spectra begin to be distinguishable (see Figure 10b). The theoretical and doping-concentration curves have the emission peak in the same wavelength ( $\hat{\lambda}_{theo} = \hat{\lambda}_{dop} = 455.8$  nm); however, the experimental peak is minimally shifted to violet (higher photon energy). This is consistent with the fact that the electron experimental mobility is higher, and therefore, their velocity and kinetic energy are also higher (for low field:  $\vec{v}_{drift} = \mu \vec{E}$ ,  $\vec{v}(\vec{k}, \vec{r}) = \frac{1}{\hbar} \nabla_k \epsilon(\vec{k}, \vec{r})$ ). This implies that the electrons reach higher eigenvalues inside the well, and thus, the energy difference released during the recombination will be higher. In Figure 10c at 3.5 V, spectra are centered again on the same wavelength ( $\hat{\lambda}_{exp} = \hat{\lambda}_{theo} = \hat{\lambda}_{dop} = 456.7$  nm). There is even a reduction of FWHM in the three plots and they have very similar values to each other. The voltage point with the most symmetrical distribution around the maximum peak and the most stable emission is 3.6 V. Since it presents the lowest FWHM ( $FWHM_{exp} = 11.1$  nm,  $FWHM_{theo} = 11.2$  nm,  $FWHM_{dop} = 11.1$  nm) and the same wavelength ( $\hat{\lambda}_{LED} = 456.7$  nm) for the three computations, it is the most likely energy transition that governs the emission. In Figure 10c, it is observed that the photon emission is higher for the experimental simulation even though Table 2 shows higher recombination in QW1, QW2 and QW3 in the theoretical simulation, so these three contributions added together do not exceed the experimental recombination value provided by the well QW4 (79.44%), as mentioned before. At the last voltage point, the emission peaks are shifted to violet and are not centered ( $\hat{\lambda}_{exp} = 446.8$  nm,  $\hat{\lambda}_{theo} = 445.2$  nm,  $\hat{\lambda}_{dop} = 449.2$  nm); moreover, there is an increase in FWHM, which indicates the presence of high energy emission peaks. The maximum violet shift and the linewidth of the emission peak with respect to the stable

wavelength for all simulations occurs at 4.0 V and its values are as follows:  $\Delta\lambda_{dop} = 7.5$  nm,  $\Delta FWHM_{dop} = 2.9$  nm;  $\Delta\lambda_{exp} = 9.9$  nm,  $\Delta FWHM_{exp} = 2.8$  nm; and  $\Delta\lambda_{theo} = 11.5$  nm,  $\Delta FWHM_{theo} = 3.1$  nm.

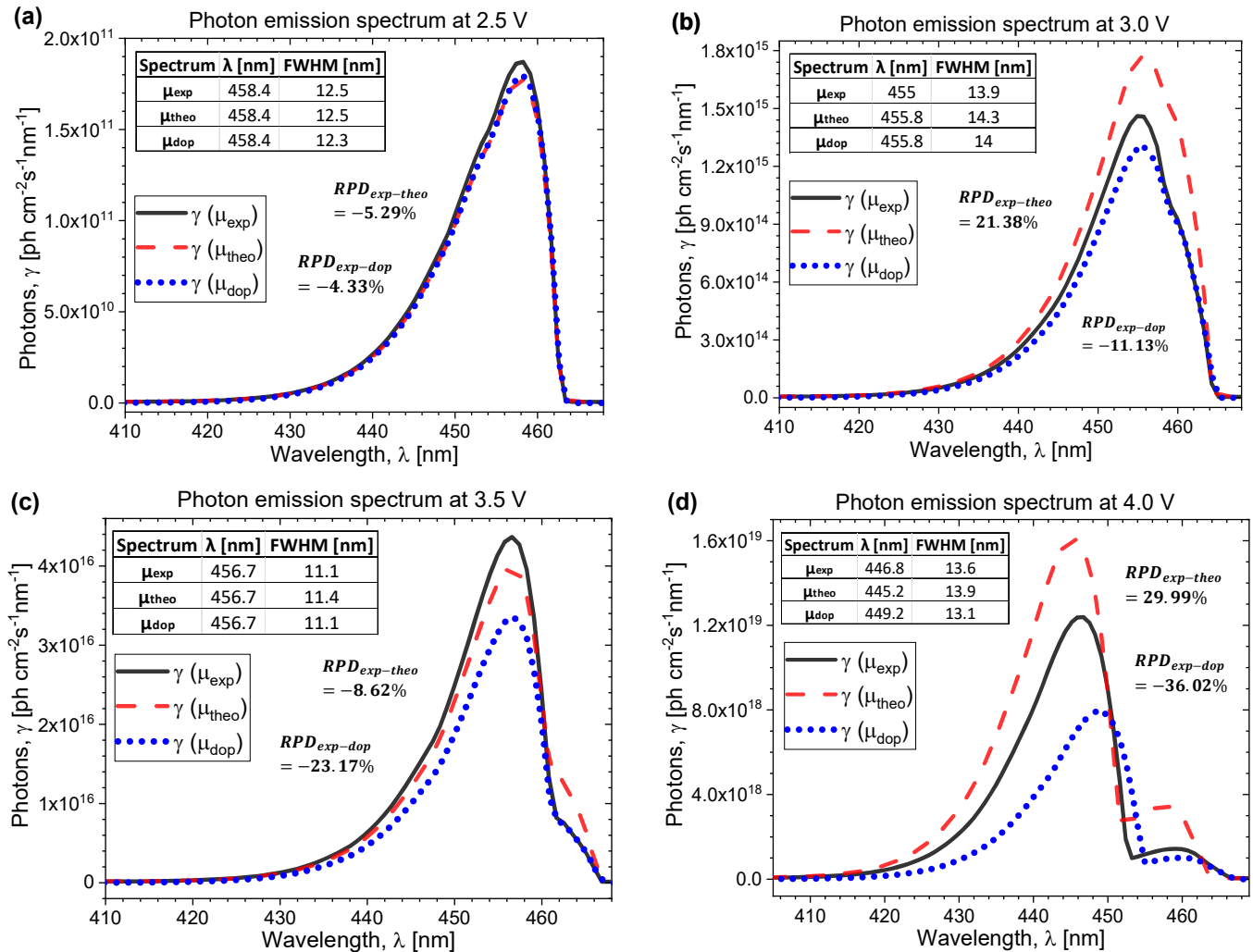


**Figure 10.** Photon emission spectrum of the LED for: (a) 2.5 V, (b) 3.0 V, (c) 3.5 V and (d) 4.0 V.

For the three simulations, the emission spectra can be explained through the energetic transitions between electron and hole states. Since the Schrödinger equation is solved for each voltage point, one different set of eigenvalues and eigenfunctions is obtained at each step. Therefore, photon emission depends on the energy difference between states and their probability via Fermi's golden rule. The most probable transitions govern the spectrum, although the transitions whose speed is greater due to their instability are also notable. Additionally, in MQWs exposed to an external electric field, the "quantum-confined Stark effect" (QCSE) appears. It is manifested by bringing the eigenenergies of the conduction and valence bands closer together, as well as by separating the electron and hole wave functions; thus, the overlap becomes less effective. All the above leads to nonlinear behavior of the emission peak, as shown in Figure 10. At this point, the emission spectrum is composed of various Lorentzian peaks corresponding to different transition energies. This is because of a higher position and less stable eigenstates of the e/h pair having a faster emission. Taking the experimental emission curve as an example, due to the band decoupling used, at low voltages (2.5 V), the main transition is between the lower states. In this case, the two transitions are:  $e_3 \rightarrow hh_3 \approx 2.71$  eV  $\approx 457.5$  nm and  $e_3 \rightarrow lh_3 \approx 2.717$  eV  $\approx 456$  nm. At 3.0 V, the electrons occupy higher energy states, and by QCSE, the eigenenergies between

$e_n \rightarrow hh_n/lh_n$  are reduced, allowing three transitions:  $e_3 \rightarrow lh_3 \approx 2.645 \text{ eV} \approx 468 \text{ nm}$ ,  $e_4 \rightarrow hh_4 \approx 2.77 \text{ eV} \approx 448 \text{ nm}$  and  $e_4 \rightarrow lh_4 \approx 2.776 \text{ eV} \approx 446 \text{ nm}$ . More energetic transitions are less stable and faster, increasing the number of photons emitted in shorter wavelengths (see the blue dotted line in Figure 11). In fact, at this voltage, the emission spectrum is wider, as illustrated by the FWHM broadening in Figure 10b. A red-shifted hump can also be seen, indicating the combination of long and short transitions in the photon spectrum. At 3.5 V, the eigenenergies are again slightly displaced by the Stark effect, and the transitions are readjusted. Transitions occurring there are:  $e_6 \rightarrow hh_6 \approx 2.695 \text{ eV} \approx 460 \text{ nm}$  and  $e_6 \rightarrow lh_6 \approx 2.7 \text{ eV} \approx 459 \text{ nm}$ . The closeness of these peak emissions causes lower FWHMs. At 4.0 V, the spectrum reveals the separation of two energy peaks; therefore, it is possible to infer four possible transitions occurring:  $e_9 \rightarrow hh_9 \approx 2.7 \text{ eV} \approx 459 \text{ nm}$ ,  $e_9 \rightarrow lh_9 \approx 2.71 \text{ eV} \approx 457.5 \text{ nm}$ ,  $e_{10} \rightarrow hh_{10} \approx 2.81 \text{ eV} \approx 441 \text{ nm}$ , and  $e_{10} \rightarrow lh_{10} \approx 2.822 \text{ eV} \approx 439 \text{ nm}$ . The deconvolution of the experimental spectrum for 3.0 V is shown in Figure 11, where more than two emission peaks are necessary to form them.

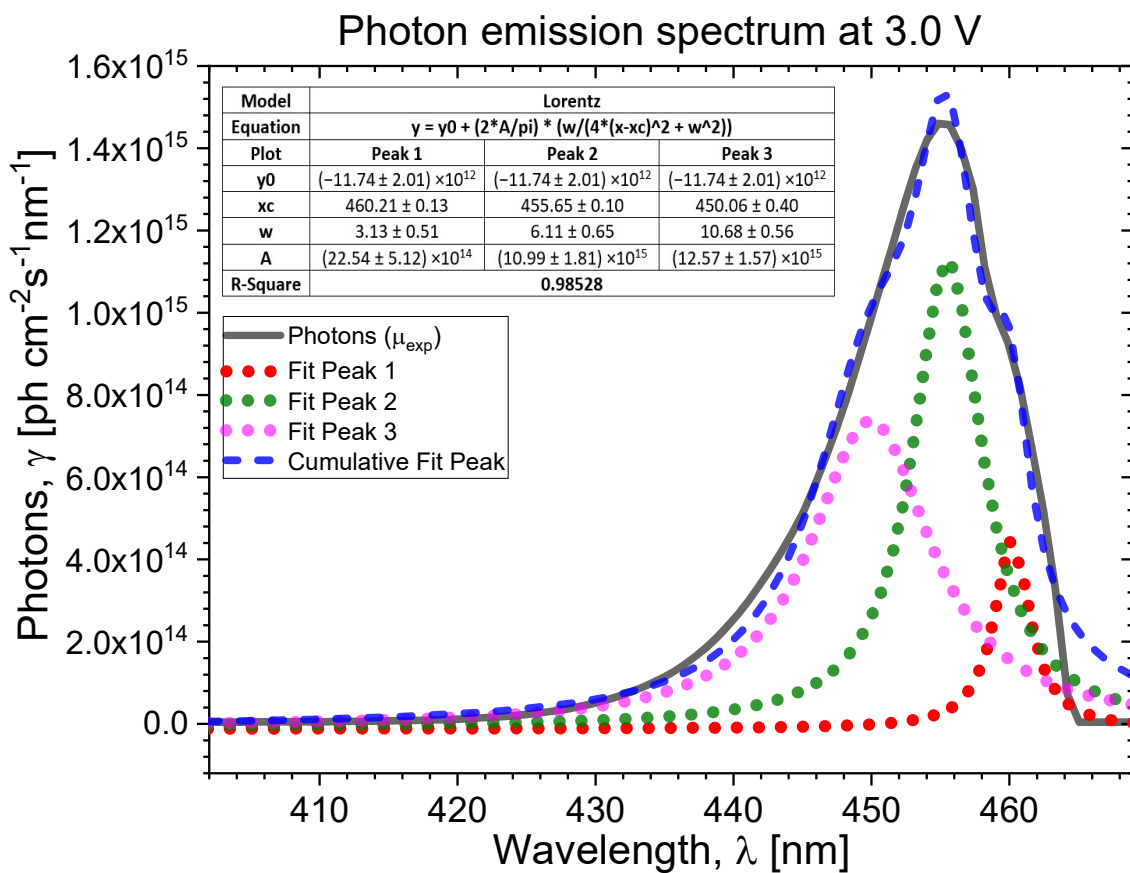


**Figure 11.** Deconvolution of the photon emission spectrum for the experimental simulation at 3.0 V.

Figure 12 shows the peak wavelength achieved for each mobility with respect to the supplied voltage (2.5–4.0) V, where it is confirmed the stable point of the emission corresponds to  $\hat{\lambda}_{LED} = 456.7 \text{ nm}$ , since all simulations take the same wavelength value and the lowest FWHMs. Therefore, in this voltage range, the SRH and Auger recombination have very similar values, and the radiative recombination is maximized as it is explained in [10,11]. Experimental computation leads to varied values of the emission peak, making it less stable. Doping-concentration simulation has a lower violet shift of the emitted wavelength at higher voltages, which makes it more stable.

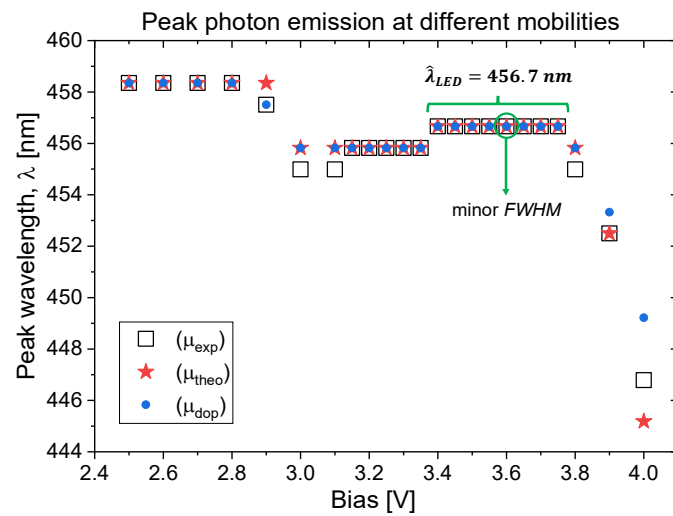


**Figure 12.** Peak photon emission for the three simulations with experimental, theoretical, and doping-concentration mobility from 2.5–4.0 V in the LED device.

Calculations of the maximum internal quantum efficiency (IQE,  $\eta_{IQE}[\%] = (J_{photo}/J_{Tot}) \times 100$ ) achieved by the three simulations occurs at the forward voltage points, being:  $\eta_{exp-max} = 57.09\%$ ,  $\eta_{theo-max} = 57.99\%$ ,  $\eta_{dop-max} = 60.43\%$ . Therefore, the doping-concentration simulation resulted in the highest  $\eta_{IQE}$  showing superiority. The typical IQE for blue LEDs in the range  $\lambda = (450-460)$  nm in the last decades has been recorded at around 60% [49,50]. Even in studies where it is attempted to improve the conventional structure, the IQE values even are around 60%. For instance, Ryu et al. [12] reported an  $\eta_{IQE} \sim 60\%$  for five periods of  $In_{0.16}Ga_{0.84}N$  MQWs with emission around  $\lambda \sim 450$  nm. The electron and hole concentrations for claddings were n-GaN =  $5 \times 10^{18} \text{ cm}^{-3}$  and p-GaN =  $5 \times 10^{17} \text{ cm}^{-3}$ . Although a doped superlattice was added to the structure, the IQE increase was low. This device is similar in composition and well number to the one studied in this work, but the electron and hole concentrations are different (n-GaN =  $1 \times 10^{17} \text{ cm}^{-3}$  and p-GaN =  $1 \times 10^{19} \text{ cm}^{-3}$ ). When Ryu uses n-GaN 50 times higher and p-GaN 20 times lower than here, its efficiency does not improve. In this way, the electron and hole concentration combination proposed in this paper seems to have more advantages, because without complicating the structure, the same performance in the device is obtained. Dong et al. [21] compares a conventional  $In_{0.2}Ga_{0.8}N$  (2.5 nm)/GaN(12.5) MQWs structure with this proposed design  $In_{0.2}Ga_{0.8}N$ (3.5 nm)/GaN(5.5) MQWs. Both LEDs consist of eleven wells, whose emission is in the range  $\lambda = (450 - 440)$  nm. The IQEs for the conventional structure and proposed design are around  $\eta_{IQE} \sim 65\%$  and  $\eta_{IQE} \sim 70\%$ , respectively. Again, electron and hole concentrations are different from those used in this study. Dong used n-GaN =  $1 \times 10^{19} \text{ cm}^{-3}$  and p-GaN =  $8 \times 10^{17} \text{ cm}^{-3}$ . This corresponds to 100 times more ionized electrons and 12 times fewer ionized holes than in this study, which also does not seem to increase efficiency substantially. Therefore, the IQE achieved by the doping-concentration mobility is comparable to those recorded by “conventional” and “improved” structures. The main difference lies in the choice of number of n-type and p-type dopants. Recent studies show that more p-type than n-type dopants increase the internal quantum efficiency ( $\sim 80\%$ ) of the device [47]. Using this approach, we will study the combination of different concentrations in future.

In summary, although the theoretical mobility generated lower electron leakage current, higher hole density, recombination rate and photon emission, these characteristics were not always the best for all voltage ranges. Therefore, it may be misleading to assume that increasing the mobility value for semiconductor materials will lead to increased optoelectronic parameters and device performance. Experimental mobility registered lower hole leakage. Although the experimental mobility represents data taken in laboratory, it does not consider other aspects influencing the dynamics transport; hence, assigning a fixed value

to mobility can affect the reliability of results. Doping-concentration mobility maintained intermediate leakage currents between the theoretical and experimental simulations. Its hole and electron densities were similar to the experimental simulation, although always below it. The recombination rate and, consequently, the photon emission remained below the other simulations; however, it showed less wavelength variation, a narrow FWHM, and the highest IQE before its breakdown voltage. Thus, doping-concentration mobility seems to be a more realistic option for device simulation. Although the mobility model used fixes the value along the simulation, this mobility includes in the calculations the variation of the electron and hole concentrations for the semiconductors, thus enriching the model without complicating it. It should be noted that the recombination coefficients ( $\tau_{SRH}$ ,  $C_{Auger}$ ,  $B_{rad}$ ) were kept constant during the simulation, and these can be adjusted to improve results and device design [10,11,51], so this area can be explored in future studies.

To conclude, care must be taken when choosing mobility values for materials since the theoretical mobility value is calculated according to basic principles and may leave out more complex physical phenomena or events generating energy dispersion. This mobility could be used for highly pure materials and devices with low defect density; however, it may not be recommended for the device's design because it would overestimate the physical parameters and their optoelectronic characteristics. On the other hand, experimental mobility values are more accurate as they are obtained from real samples, although using them deliberately without knowing what physical parameters are changing transport dynamics in the device may produce erroneous results when predictions are made by simulation. Finally, adjusting the mobility values according to the electron and hole concentrations, as was done in this study, is the best option to strengthen the analysis without complicating the computational calculations.

#### 4. Conclusions

Simulations on mobility influence in optoelectronics parameters from an InGaN/GaN blue LED using the Nextnano++ software were presented in this paper. These simulations were performed by changing the hole and electron mobility value for the material compounds according to experimental, theoretical, and doping-concentration data. The power law mobility was used for the current calculation in the quantum drift-diffusion model. The results exhibit significant changes in the energy transport and dispersion mechanisms in the range of (2.5–4.1) volts, where an analysis of the physical parameters was carried out. The lower hole and electron leakage currents correspond to the lowest mobility values for the InGaN alloy, suggesting that a lower mobility for this material favors the permanence of the e/h pairs in the well increasing the recombination probability and thereby the device emission. The greatest amount of recombination occurs in the extreme wells within the active layer of the LED throughout the voltage sweep, regardless of the mobility value. The stable emission is at 3.6 V, with peak wavelength  $\lambda_{LED} = 456.7$  nm and  $FWHM \sim 11.1$  nm for the three mobilities. The maximum violet shift of the wavelength peak and the broadening of the spectral line reveals that the doping-concentration mobility produces the most stable emission. The highest quantum efficiency was achieved by doping-concentration mobility ( $\eta_{dop-max} = 60.43\%$ ), making it superior to the others and achieving similar efficiencies to other conventional devices.

**Author Contributions:** Conceptualization, S.Z.-G. and A.G.-B.; methodology, O.P.-C. and S.Z.-G.; software, S.Z.-G.; validation, A.G.-B. and S.Z.-G.; formal analysis, A.G.-B., S.Z.-G. and R.A.-L.; investigation, J.H.-M. and S.Z.-G.; resources, J.P.-C.; data curation, O.P.-C. and S.Z.-G.; writing—original draft preparation, S.Z.-G.; writing—review and editing, M.G.-R.; visualization, E.S.-N.; supervision, A.G.-B.; project administration, O.P.-C.; funding acquisition, J.P.-C. All authors have read and agreed to the published version of the manuscript.

**Funding:** This work was supported in part by CONACyT Mexico under Grants 319712, 169062, 204419, 626570, and PRODEP Mexico.

**Institutional Review Board Statement:** Not applicable.

**Informed Consent Statement:** Not applicable.

**Data Availability Statement:** Details about the data used and where they can be found are provided in Table 1.

**Acknowledgments:** The authors would like to warmly thank the reviewers for their relevant comments that helped in clarifying and improving the content of the paper.

**Conflicts of Interest:** The authors declare no conflict of interest.

## References

1. Trellakis, A.; Galick, A.T.; Pacelli, A.; Ravaoli, U. Iteration scheme for the solution of the two-dimensional Schrödinger-Poisson equations in quantum structures. *J. Appl. Phys.* **2007**, *81*, 7880–7884. [CrossRef]
2. Sabathil, M.; Hackenbuchner, S.; Majewski, J.A.; Zandler, G.; Vogl, P. Towards fully quantum mechanical 3D device simulations. *J. Comput. Electron.* **2002**, *1*, 81–85. [CrossRef]
3. Auf der Maur, M.; Povolotskiy, M.; Sacconi, F.; Pecchia, A.; Romano, G.; Penazzi, G.; Di Carlo, A. TiberCAD: Towards multiscale simulation of optoelectronic devices. *Opt. Quant. Electron.* **2008**, *40*, 1077–1083. [CrossRef]
4. Li, K.H.; Fu, W.Y.; Cheung, Y.F.; Wong, K.K.Y.; Wang, Y.; Lau, K.M.; Choi, H.W. Monolithically integrated InGaN/GaN light-emitting diodes, photodetectors, and waveguides on Si substrate. *Optica* **2018**, *5*, 564–569. [CrossRef]
5. Chen, J.; Wang, J.; Ji, K.; Jiang, B.; Cui, X.; Sha, W.; Wang, B.; Dai, X.; Hua, Q.; Wan, L.; et al. Flexible, stretchable, and transparent InGaN/GaN multiple quantum wells/polyacrylamide hydrogel-based light emitting diodes. *Nano Res.* **2022**, *15*, 5492–5499. [CrossRef]
6. Li, Y.; Liu, C.; Zhang, Y.; Jiang, Y.; Hu, X.; Song, Y.; Su, Z.; Jia, H.; Wang, W.; Chen, H. Realizing Single Chip White Light InGaN LED via Dual-Wavelength Multiple Quantum Wells. *Materials* **2022**, *15*, 3998. [CrossRef]
7. Cai, L.-E.; Zhang, B.-P.; Lin, H.-X.; Cheng, Z.-J.; Ren, P.-P.; Chen, Z.-C.; Huang, J.-M.; Cai, L.-L. Effect of barrier thickness on photoelectric properties of InGaN/GaN asymmetric multiple-quantum-well structure light-emitting diode. *AIP Adv.* **2022**, *12*, 65007. [CrossRef]
8. Wang, Y.; Liang, F.; Zhao, D.; Ben, Y.; Yang, J.; Liu, Z.; Chen, P. Effect of High Temperature Treatment on the Photoluminescence of InGaN Multiple Quantum Wells. *Crystals* **2022**, *12*, 839. [CrossRef]
9. Zhang, Z.H.; Tan, S.T.; Ji, Y.; Liu, W.; Ju, Z.; Kyaw, Z.; Demir, H.V. A PN-type quantum barrier for InGaN/GaN light emitting diodes. *Opt. Express* **2013**, *21*, 15676–15685. [CrossRef]
10. Bulashevich, K.A.; Khokhlev, O.V.; Evstratov, I.Y.; Karpov, S.Y. Simulation of light-emitting diodes for new physics understanding and device design. *Proc. SPIE* **2012**, *8278*, 827819.
11. Jia, X.; Zhou, Y.; Liu, B.; Lu, H.; Xie, Z.; Zhang, R.; Zheng, Y. A simulation study on the enhancement of the efficiency of GaN-based blue light-emitting diodes at low current density for micro-LED applications. *Mater. Res. Express* **2019**, *6*, 105915. [CrossRef]
12. Ryu, H.-Y.; Choi, W.J. Optimization of InGaN/GaN superlattice structures for high-efficiency vertical blue light-emitting diodes. *J. Appl. Phys.* **2013**, *114*, 173101. [CrossRef]
13. Birner, S.; Hackenbuchner, S.; Sabathil, M.; Zandler, G.; Majewski, J.A.; Andlauer, T.; Vogl, P. Modeling of Semiconductor Nanostructures with nextnano. *Acta Phys. Pol. A* **2006**, *110*, 111. [CrossRef]
14. Trellakis, A.; Zibold, T.; Andlauer, T.; Birner, S.; Smith, R.K.; Morschl, R.; Vogl, P. The 3D nanometer device project nextnano: Concepts, methods, results. *J. Comput. Electron.* **2006**, *5*, 285–289. [CrossRef]
15. Birner, S.; Zibold, T.; Andlauer, T.; Kubis, T.; Sabathil, M.; Trellakis, A.; Vogl, P. Nextnano: General Purpose 3-D Simulations. *IEEE Trans. Electron Devices* **2007**, *54*, 2137–2142. [CrossRef]
16. Nextnano; München, Germany. Available online: <https://www.nextnano.com/index.php> (accessed on 25 June 2022).
17. Brochen, S.; Brault, J.; Chenot, S.; Dussaigne, A.; Leroux, M.; Damilano, B. Dependence of the Mg-related acceptor ionization energy with the acceptor concentration in p-type GaN layers grown by molecular beam epitaxy. *Appl. Phys. Lett.* **2013**, *103*, 269904. [CrossRef]
18. Wang, H.; Chen, A.-B. Calculations of acceptor ionization energies in GaN. *Phys. Rev. B* **2001**, *63*, 125212. [CrossRef]
19. Hernández-Gutiérrez, C.A.; Casallas-Moreno, Y.L.; Rangel-Kuoppa, V.-T.; Cardona, D.; Hu, Y.; Kudriatsev, Y.; Zambrano-Serrano, M.A.; Gallardo-Hernandez, S.; Lopez-Lopez, M. Study of the heavily p-type doping of cubic GaN with Mg. *Sci. Rep.* **2006**, *10*, 16858. [CrossRef]
20. Amano, H. Growth of GaN on sapphire via low-temperature deposited buffer layer and realization of p-type GaN by Mg doping followed by low-energy electron beam irradiation (Nobel Lecture). *Ann. Phys.* **2015**, *527*, 327–333. [CrossRef]
21. Dong, H.; Jia, T.; Liang, J.; Zhang, A.; Jia, Z.; Jia, W.; Liu, X.; Li, G.; Wu, Y.; Xu, B. Improved carrier transport and photoelectric properties of InGaN/GaN multiple quantum wells with wider well and narrower barrier. *Opt. Laser Technol.* **2020**, *129*, 106309. [CrossRef]
22. Greck, P.; Birner, S.; Huber, B.; Vogl, P. Efficient method for the calculation of dissipative quantum transport in quantum cascade lasers. *Opt. Express* **2015**, *23*, 6587–6600. [CrossRef] [PubMed]
23. Andlauer, T. Optoelectronic and Spin-Related Properties of Semiconductor Nanostructures in Magnetic Fields. Ph.D. Dissertation, Technische Universität München, Munich, Germany, 2009.

24. Li, S. The Atomic Structure of Inversion Domains and Grain Boundaries in Wurtzite Semiconductors: An Investigation by Atomistic Modelling and High-Resolution Transmission Electron Microscopy. Ph.D. Dissertation, Normandie Université, Caen, France, 2018.
25. Henini, M.; Razeghi, M. *Optoelectronic Devices: III Nitrides*; Elsevier: Oxford, UK, 2004; pp. 9–18.
26. Martin, G.; Botchkarev, A.; Rockett, A.; Morkoc, H. Valence-band discontinuities of wurtzite GaN, AlN, and InN heterojunctions measured by X-ray photoemission spectroscopy. *Appl. Phys. Lett.* **1996**, *68*, 2541–2543. [[CrossRef](#)]
27. Bernardini, F.; Fiorentini, V. Spontaneous versus piezoelectric polarization in III–V nitrides: Conceptual aspects and practical consequences. *Phys. Stat. Sol.* **1999**, *216*, 391–398. [[CrossRef](#)]
28. Park, S.-H. Crystal Orientation Effects on Electronic Properties of Wurtzite GaN/AlGaIn Quantum Wells with Spontaneous and Piezoelectric Polarization. *Jpn. J. Appl. Phys.* **2000**, *39*, 3478–3482. [[CrossRef](#)]
29. Schulz, T.; Lymperakis, L.; Anikeeva, M.; Siekacz, M.; Wolny, P.; Markurt, T.; Albrecht, M. Influence of strain on the indium incorporation in (0001) GaN. *Phys. Rev. Mater.* **2020**, *4*, 73404. [[CrossRef](#)]
30. Quay, R.; Moglestue, C.; Palankovski, V.; Selberherr, S. A temperature dependent model for the saturation velocity in semiconductor materials. *Mater. Sci. Semicond. Process.* **2000**, *3*, 149–155. [[CrossRef](#)]
31. Lane, D.; Hayne, M. Simulations of Ultralow-Power Nonvolatile Cells for Random-Access Memory. *IEEE Trans. Electron. Devices* **2020**, *67*, 474–480. [[CrossRef](#)]
32. COMSOL Multiphysics; Massachusetts, USA. Available online: <https://doc.comsol.com/5.5/doc/com.comsol.help.semicond/semicond Ug semiconductor.6.52.html> (accessed on 25 June 2022).
33. Kyle, E.C.H.; Kaun, S.W.; Burke, P.G.; Wu, F.; Wu, Y.-R.; Speck, J.S. High-electron-mobility GaN grown on free-standing GaN templates by ammonia-based molecular beam epitaxy. *J. Appl. Phys.* **2014**, *115*, 193702. [[CrossRef](#)]
34. Poncé, S.; Jena, D.; Giustino, F. Hole mobility of strained GaN from first principles. *Phys. Rev. B* **2019**, *100*, 085204. [[CrossRef](#)]
35. Arakawa, Y.; Ueno, K.; Imabeppu, H.; Kobayashi, A.; Ohta, J.; Fujioka, H. Electrical properties of Si-doped GaN prepared using pulsed sputtering. *Appl. Phys. Lett.* **2017**, *110*, 042103. [[CrossRef](#)]
36. Horita, M.; Takashima, S.; Tanaka, R.; Matsuyama, H.; Ueno, K.; Edo, M.; Suda, J. Hall-effect measurements of metalorganic vapor-phase epitaxy-grown p-type homoepitaxial GaN layers with various Mg concentrations. *Jpn. J. Appl. Phys.* **2017**, *56*, 031001. [[CrossRef](#)]
37. Yarar, Z. Transport and mobility properties of wurtzite InN and GaN. *Phys. Status Solidi* **2007**, *244*, 3711–3718. [[CrossRef](#)]
38. Chen, F.; Cartwright, A.N.; Lu, H.; Schaff, W.J. Ultrafast carrier dynamics in InN epilayers. *J. Cryst. Growth* **2004**, *269*, 10–14. [[CrossRef](#)]
39. AZoM, Riyadh, Saudi Arabia. Available online: <https://www.azom.com/article.aspx?ArticleID=8367>. (accessed on 25 June 2022).
40. Chen, F.; Cartwright, A.N.; Lu, H.; Schaff, W.J. Hole transport and carrier lifetime in InN epilayers. *Appl. Phys. Lett.* **2005**, *87*, 21210. [[CrossRef](#)]
41. Ma, N.; Wang, X.Q.; Liu, S.T.; Chen, G.; Pan, J.H.; Feng, L.; Shen, B. Hole mobility in wurtzite InN. *Appl. Phys. Lett.* **2011**, *98*, 192114. [[CrossRef](#)]
42. Piprek, J. *Nitride Semiconductor Devices: Principles and Simulation*; John Wiley & Sons: Weinheim, Germany, 2007.
43. Shen, Y.C.; Mueller, G.O.; Watanabe, S.; Gardner, N.F.; Munkholm, A.; Krames, M. Auger recombination in InGaIn measured by photoluminescence. *Appl. Phys. Lett.* **2007**, *91*, 141101. [[CrossRef](#)]
44. Dmitriev, A.; Oruzhenikov, A. The rate of radiative recombination in the nitride semiconductors and alloys. *J. Appl. Phys.* **2017**, *86*, 3241–3246. [[CrossRef](#)]
45. Kioupakis, E.; Yan, Q.; Steiauf, D.; Van de Walle, C. Temperature and carrier-density dependence of Auger and radiative recombination in nitride optoelectronic devices. *New J. Phys.* **2013**, *15*, 125006. [[CrossRef](#)]
46. Lee, M.; Yang, M.; Song, K.M.; Park, S. InGaIn/GaN Blue Light Emitting Diodes Using Freestanding GaN Extracted from a Si Substrate. *ACS Photonics* **2018**, *5*, 1453–1459. [[CrossRef](#)]
47. Lu, S.; Li, J.; Huang, K.; Liu, G.; Zhou, Y.; Cai, D.; Zhang, R.; Kang, J. Additional file 1 of Designs of InGaIn Micro-LED Structure for Improving Quantum Efficiency at Low Current Density. *Nanoscale Res. Lett.* **2021**, *16*, 99. [[CrossRef](#)]
48. Chen, J.R.; Wu, Y.C.; Ling, S.C.; Ko, T.S.; Lu, T.C.; Kuo, H.C.; Wang, S.C. Investigation of wavelength-dependent efficiency droop in InGaIn light-emitting diodes. *Appl. Phys. B* **2010**, *98*, 779–789. [[CrossRef](#)]
49. Jae-Hyun, R.; Yoder, P.D.; Jianping, L.; Lochner, Z.; Hyunsoo, K.; Suk, C.; Hee, J.K.; Dupuis, R.D. Control of quantum-confined stark effect in InGaIn-based quantum wells. *IEEE J. Sel. Top. Quant.* **2009**, *15*, 1080–1091. [[CrossRef](#)]
50. Zhou, Q.; Xu, M.; Wang, H. Internal quantum efficiency improvement of InGaIn/GaN multiple quantum well green light-emitting diodes. *Opto-Electron. Rev.* **2016**, *24*, 1–9. [[CrossRef](#)]
51. Cho, J.; Schubert, E.F.; Kim, J.K. Efficiency droop in light-emitting diodes: Challenges and countermeasures. *Laser Photonics Rev.* **2013**, *7*, 408–421. [[CrossRef](#)]